

Broadband polarization-independent terahertz multifunctional liquid crystal coding metasurface based on topological optimization

Yu Chen(陈羽), Wu-Hao Cao(曹昊昊), Jia-Qi Li(李嘉琦), Ming-Zhe Zhang(张明哲), Xin-Yi Du(杜欣怡), Ding-Shan Gao(郜定山), and Pei-Li Li(李培丽)

Citation: Chin. Phys. B, 2025, 34 (**4**): 044205. DOI: 10.1088/1674-1056/adad55
Journal homepage: http://cpb.iphy.ac.cn; http://iopscience.iop.org/cpb

What follows is a list of articles you may be interested in

Tailoring topological corner states in photonic crystals by near- and far-field coupling effects

Zhao-Jian Zhang(张兆健), Zhi-Hao Lan(兰智豪), Huan Chen(陈欢), Yang Yu(于洋), and Jun-Bo Yang(杨俊波)
Chin. Phys. B, 2023, 32 (**12**): 124201. DOI: 10.1088/1674-1056/acddd3

Efficient manipulation of terahertz waves by multi-bit coding metasurfaces and further applications of such metasurfaces

Yunping Qi(祁云平) Baohe Zhang(张宝和), Jinghui Ding(丁京徽), Ting Zhang(张婷), Xiangxian Wang(王向贤), and Zao Yi(易早)
Chin. Phys. B, 2021, 30 (**2**): 024211. DOI: 10.1088/1674-1056/abd6fc

Polarization-independent silicon photonic grating coupler for large spatial light spots

Lijun Yang(杨丽君), Xiaoyan Hu(胡小燕), Bin Li(李斌), and Jing Cao(曹静)
Chin. Phys. B, 2021, 30 (**2**): 024206. DOI: 10.1088/1674-1056/abbc00

Polarization-insensitive complementary metamaterial structure based on graphene for independently tuning multiple transparency windows

Hailong Huang(黄海龙), Hui Xia(夏辉), and Hongjian Li(李宏建)
Chin. Phys. B, 2020, 29 (**11**): 114203. DOI: 10.1088/1674-1056/abb307

Pancharatnam-Berry metasurface for terahertz wave radar cross section reduction

Shao-He Li(李绍和), Jiu-Sheng Li(李九生)
Chin. Phys. B, 2019, 28 (**9**): 094210. DOI: 10.1088/1674-1056/ab33f5

Broadband polarization-independent terahertz multifunctional liquid crystal coding metasurface based on topological optimization

Yu Chen(陈羽)[1], Wu-Hao Cao(曹吴昊)[1], Jia-Qi Li(李嘉琦)[1], Ming-Zhe Zhang(张明哲)[1], Xin-Yi Du(杜欣怡)[1], Ding-Shan Gao(郜定山)[2], and Pei-Li Li(李培丽)[1,†]

[1] *Nanjing University of Posts and Telecommunications, Nanjing* 210003, *China*
[2] *Wuhan National Laboratory for Optoelectronics, College of Optoelectronic Science and Engineering, Huazhong University of Science and Technology, Wuhan* 430074, *China*

(Received 19 December 2024; revised manuscript received 13 January 2025; accepted manuscript online 23 January 2025)

A broadband polarization-independent terahertz multifunctional coding metasurface based on topological optimization using liquid crystal (LC) is proposed. The metasurface can achieve reconfigurability for beam steering and vortex beam generation within a frequency range of 0.68 THz–0.72 THz. Firstly, the metasurface unit is topologically optimized using the non-dominant sequencing genetic algorithms (NSGA-II) multi-objective optimization algorithm. By applying the LC's electrically tunable refractive index properties, the metasurface unit enables polarization-independent 2-bit coding within a frequency range of 0.68 THz–0.72 THz. Then, based on the designed metasurface unit, the array arrangement of the metasurface is reverse-designed to achieve beam steering and vortex beam generation. The results show that, for beam steering, not only can polarization-independent steering of both single- and multi-beam be achieved within the 35° elevation angle range, but also independent control of the target angle of each beam in the multi-beam steering. For vortex beam generation, the metasurfaces can achieve the generation of single- and multi-vortex beams with topological charges $l = \pm 1$, ± 2 within the 35° elevation angle range, and the generation angles of each vortex beam in the multi-vortex beam can be independently controlled. This provides flexibility and diversity in the generation of vortex beams. Therefore, the proposed terahertz LC metasurface can realize flexible control of reconfigurable functions and has certain application prospects in terahertz communication, phased array radar, and vortex radar.

Keywords: coding metasurfaces, polarization-independent, terahertz, topology optimization

PACS: 02.40.Pc, 42.70.Df, 61.30.–v, 07.05.Tp, 42.25.Bs

DOI: 10.1088/1674-1056/adad55 **CSTR:** 32038.14.CPB.adad55

1. Introduction

Terahertz (THz) waves are widely used in radar, remote sensing, and data transmission due to their advantages of low loss and high penetration capability. THz manipulation is the cornerstone for realizing these applications and has been extensively studied. Metasurfaces are artificial subwavelength materials capable of strongly manipulating incident electromagnetic waves, and have advantages such as thin thickness, low loss, small volume, and easy integration, which are widely used in THz manipulation.

In 2014, Cui *et al.*[1] proposed the concept of digitally coding metasurfaces, improving electromagnetic wave manipulation ability. Different array arrangements of coding metasurface can achieve various functions, such as beam steering, vortex beam generation, and RCS reduction.[2–6] Coding metasurfaces can be categorized into two types in the THz band according to whether dynamic coding can be achieved. The first type is structural coding metasurfaces which can achieve coding by changing the structure of the metasurface unit. The second type is tunable materials coding metasurfaces which can achieve coding by changing the tunable material parameters of the metasurface unit. For the structural metasurfaces, their functionalities are uniquely determined once fabricated, which restricts their applications.[7] With the development of modern devices, multifunctional reconfigurable metasurface devices that can integrate multiple functions become a research hotspot. The tunable materials coding metasurfaces, due to the introduction of tunable materials, such as LC, graphene, vanadium dioxide (VO_2), and Dirac semimetals, can achieve dynamic manipulation of THz waves under external control.[8,9] Therefore, the tunable materials coding metasurfaces have reconfigurable multifunctionality and have become the mainstream solution for THz coding metasurfaces.

An asymmetric resonant "C" ring LC metasurface was designed[10] to achieve 1-bit coding at 0.408 THz, enabling double beam steering and vortex beam generation with different topological charges in the range of 31.9°. A graphene metasurface was proposed,[11] which can achieve 1-bit coding at 1 THz, and realize double-beam and four-beam steering within 30° of elevation angle. A metasurface based on Dirac semi-metal was proposed,[12] capable of 3-bit coding at 1.1 THz, and realizing beam steering in the range of 16.9° elevation angle, vortex beam generation with different topo-

†Corresponding author. E-mail: lipl@njupt.edu.cn

© 2025 Chinese Physical Society and IOP Publishing Ltd. All rights, including for text and data mining, AI training, and similar technologies, are reserved.

logical charges, and RCS reduction greater than 10 dB in the frequency band of 0.8 THz–1.1 THz. An LC metasurface using topological optimization was designed,[13] which achieves 2-bit coding at 0.394 THz and realizes single and multi-beam steering within a 30° elevation angle range and the generation of single and multi-vortex beams. A bilayer ring-shaped metasurface based on Dirac semimetals was proposed,[14] capable of achieving 2-bit coding at 1.95 THz, realizing single and multi-beam steering within a 40° range and the generation of single and multi-vortex beam, and RCS reduction greater than 10 dB in the frequency band of 1.72 THz–2.51 THz. A VO_2 ring metasurface was proposed,[15] which can achieve 1-bit coding in the frequency range of 0.735 THz–0.965 THz, and realize double beam steering in the elevation angle of 43° and polarization conversion at 90% polarization conversion. A VO_2 metasurface was proposed,[16] which can achieve 1-bit coding in the frequency range of 0.218 THz–0.232 THz, and realize double beam steering in the elevation angle of 53°.

In summary, by introducing tunable materials, metasurfaces can achieve reconfigurability between different functions. However, the metasurfaces proposed in the aforementioned literature can only encode THz waves with a single polarization direction. Most of these metasurfaces achieve either multi-bit coding at a single frequency point or 1-bit coding within a certain frequency range. For the beam steering, the metasurface suffers from the limitations of uncontrollable beam numbers and inflexible beam steering angles due to the use of gradient phase and checkerboard coding methods. For the vortex beam generation, there are drawbacks such as the uncontrollable number of vortex beams, limited flexibility in the generation angles, and a lack of diversity in the topological charge numbers of the generated vortex beams.

Topology optimization is a mathematical method that utilizes optimization algorithms to reverse design the material distribution. In topologically optimized metasurfaces, the metasurface units are discretized into equal pixels, and these pixels are optimized as variables, which enhances both the design freedom and the design efficiency of the metasurface units. This method enhances design flexibility and achieves superior performance. A broadband polarization conversion unit with high transmittance was designed using a multi-feature topology optimization method based on the differential evolution (DE) algorithm.[17] A 3-bit coding unit was designed employing a powerful combination of genetic algorithms (GA) and finiteelement analysis programs.[18] A metasurface absorber with improved performance was designed through topology optimization using particle swarm optimization.[19,20]

In this paper, we propose a broadband polarization-independent LC 2-bit coding metasurface based on topology optimization, which enables reconfigurability for both beam steering and vortex beam generation within a certain frequency range. Firstly, aiming to achieve polarization-independent 2-bit coding, the LC coding metasurface unit is reverse-designed based on topology optimization. Then, based on the scattering principle of digital encoding metasurfaces, the array arrangement of the metasurface is reverse-designed using the NSGA-II multi-objective optimization algorithm to achieve beam steering and vortex beam generation. Finally, full-wave simulation is conducted for beam steering and vortex beam generation. To evaluate the effectiveness of the array arrangement obtained from the reverse design in achieving beam steering and vortex beam generation, the elevation angle control range, angular error of the target beams, and scattering intensity within a certain frequency range for single- and multi-beam are analyzed and calculated.

2. Unit structure design and analysis of theory

2.1. Unit structure design

The schematic diagram of the structure of the LC coding metasurface unit is illustrated in Fig. 1. It consists of a quartz layer, a metal ground layer, a polyimide (PI) layer, an LC layer, and a surface metal pattern layer. The bottom and top quartz layers serve as the support material for the unit, with a dielectric constant of 3.78 and a tangent loss of 0.002. The intermediate layer LC is nematic LC. Under different applied bias voltages, the LC molecules exhibit varying response states, resulting in different effective dielectric constants for the LC. The metal ground layer and the surface metal pattern layer are copper, which is used to generate metal resonance effects and serve as electrodes to apply bias voltages to the LC layer. The conductivity of copper is $\sigma_{\text{copper}} = 5.8 \times 10^7$ S/m. The PI layer, spin-coated on the inner side of the metal layer, functions as an orientation layer to control the alignment of LC molecules through friction.

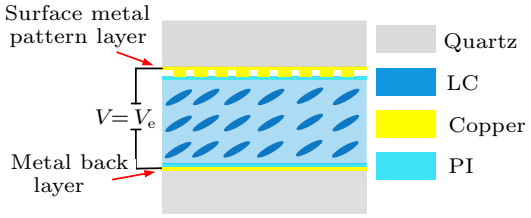


Fig. 1. Schematic diagram of the structure of the LC coding metasurface unit at a bias voltage of V_e.

2.2. Analysis of theory

The effective dielectric constant of the LC material can be expressed as[21]

$$\varepsilon = \frac{\varepsilon_\perp \varepsilon_\parallel}{\varepsilon_\perp \sin^2 \psi + \varepsilon_\parallel \cos^2 \psi}, \tag{1}$$

where ψ is the deflection angle of LC molecules under different bias voltages. $\varepsilon_\perp$ is the effective dielectric constant of the

LC when no bias voltage is applied, where the long axes of the LC molecules are perpendicular to the direction of the applied electric field. $\varepsilon_{\parallel}$ is the effective dielectric constant of the LC when a saturation bias voltage $V_{\rm th}$ is applied, where the long axes of the LC molecules are parallel to the direction of the applied electric field. By varying the applied voltage $V_{\rm e} \in [0, V_{\rm th}]$, the LC molecules will deflect at different angles, and the dielectric constant of the LC can be continuously adjusted between $\varepsilon_{\perp}$ and $\varepsilon_{\parallel}$. In this paper, the HFUT-HB01 nematic LC is selected. Within the frequency range of 0 THz–2.5 THz, when the applied bias voltage is 0 V–10 V, its adjustable range of dielectric constant is 2.47–3.60, and the loss tangent is 0.02.[22] Dynamic control of the dielectric constant of LC units can be achieved by applying different voltages to the units using field-programmable gate array (FPGA) technology.[23]

For the normal incidence of plane waves, the far-field scattering intensity of the coding metasurfaces can be expressed as[1]

$$f(\theta,\varphi) = f_{\rm e}(\theta,\varphi)\sum_{m=1}^{M}\sum_{n=1}^{N}\exp\left\{-{\rm i}\left\{\phi(m,n)+KD\sin\theta \times\left[\left(m-\frac{1}{2}\right)\cos\varphi+\left(n-\frac{1}{2}\right)\sin\varphi\right]\right\}\right\}, \quad (2)$$

where θ is the elevation angle, φ is the azimuth angle, $f_{\rm e}(\theta,\varphi)$ is the unit's far-field function, K is the propagation constant, D is the period size of a metasurface unit, and $\phi(m,n)$ is the phase response of the metasurface unit positioned at (m, n) on the metasurface.

According to Eq. (2), flexible manipulation of electromagnetic waves can be achieved by setting different phase response $\phi(m,n)$ of the metasurface units. Therefore, for the beam steering, according to the target angles ($\theta_{\rm obj}$, $\varphi_{\rm obj}$), the phase response $\phi(m,n)$ of the unit is designed to maximize $|f(\theta_{\rm obj},\varphi_{\rm obj})|$ by using optimization algorithm. The resulting distribution of $\phi(m,n)$ constitutes the optimal array arrangement of the metasurface for achieving the desired angle control. By employing optimization algorithms to inverse design metasurface array arrangement, the design efficiency can be enhanced, which enables the manipulation of metasurfaces more proactive and flexible.

According to the convolution principle of the vortex beam, a vortex beam with the same exit angle can be generated by convolving the vortex phase with a regular beam emitted at a specific angle. Hence, it is possible to achieve the generation of a vortex beam at different target angles using this method. The vortex phase typically divides the surface into N different regions, each with a phase distribution that satisfies

$$\phi_m(x,y) = \frac{2\pi}{N}\left(\frac{l\cdot\tan^{-1}(y/x)}{2\pi/N}+1\right), \quad (3)$$

where N is the number of partitions for the metasurface, l is the topological charge of the OAM wave, and (x,y) is the two-dimensional coordinates of the metasurface unit. Figure 2 illustrates the vortex phase distributions for topological charge $l = \pm1$, and ±2, respectively.

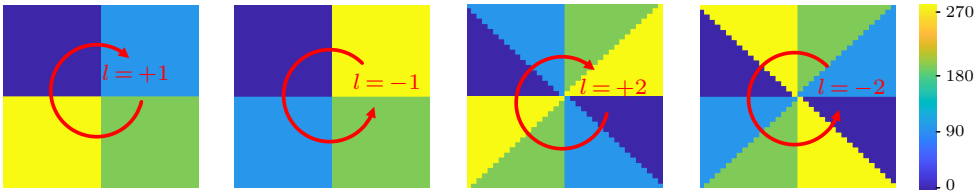


Fig. 2. Diagrams of vortex phase distribution for topological charges $l = \pm1$, ±2 respectively.

3. Results and discussion

3.1. Topology optimization design of unit structure

Topology optimization is conducted on the surface metal pattern layer of the metasurface unit. In this study, the surface metal pattern layer is partitioned into four quadrants and further subdivided in the first quadrant into 9×9 equally sized pixels. Metallic and non-metallic pixels correspond to '1' and '0' in binary, respectively. To ensure the polarization independence of the metasurface unit and enhance convergence speed, the coded first quadrant is rotated counterclockwise by 90° three times to generate the entire surface metal pattern layer with central symmetry, which can make the metasurface unit polarization-independent. Simultaneously, the periodicity D of the unit structure, the thickness $H_{\rm lc}$ of the LC layer, and the thickness $H_{\rm q}$ of the quartz layer are also optimized as variables. According to empirical values of the design structure parameters, the optimization ranges are set as follows: D is 220 μm–250 μm, $H_{\rm lc}$ is 10 μm–70 μm, and $H_{\rm q}$ is 30 μm–130 μm.

In this paper, we focu on the reverse design of a 2-bit LC coding unit within a certain frequency range. Two of the four encoding states correspond to the critical states in which no voltage and the maximum bias voltage are applied to the LC layer (the dielectric constants of LC are 2.47 and 3.60, respectively). The dielectric constants of the remaining two states are treated as variables to be optimized. The optimization process involves four objectives: achieving an average phase difference of 90° between the 0/1, 1/2, and 2/3 states within the target frequency band, and ensuring equal amplitude between the 0/1/2/3 states. Although single-objective op-

timization algorithms can address multi-objective problems by using a weighting method, the final result is significantly influenced by the choice of weights, making it difficult to obtain the desired optimal solution. The NSGA-II multi-objective optimization algorithm can improve convergence speed and optimization efficiency by employing an elitist strategy and fast non-dominated sorting, and has demonstrated significant advantages in the field of multi-objective optimization. Therefore, we choose the NSGA-II multi-objective optimization algorithm to design the coding metasurface unit.

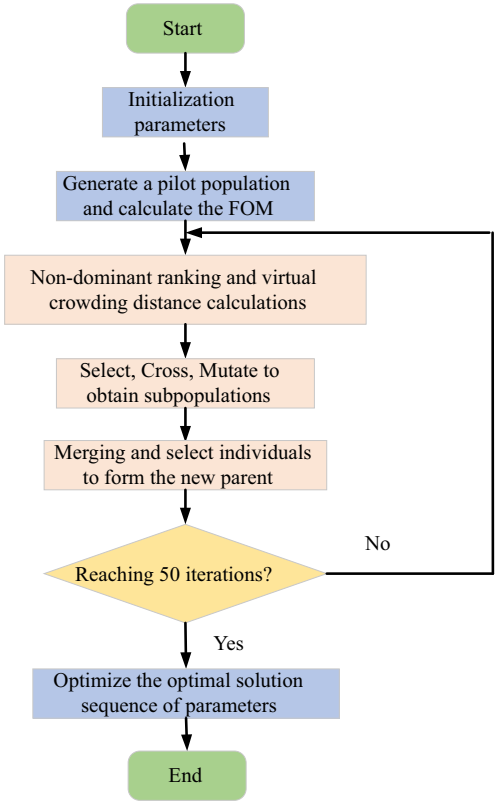


Fig. 3. Flow diagram of reverse design metasurface unit based on NSGA-II.

In this paper, the specific process of using the algorithm to design the metasurface unit inversely is illustrated in Fig. 3. Firstly, the optimization parameters for the metasurface unit are initialized: the population size is set to 50, the number of iterations is set to 50, and the fitness function is defined as

$$\min\begin{cases} f_1 = \dfrac{\sum_{i=1}^{\text{size}} (90 - |\varphi_{i0} - \varphi_{i1}|)^2}{\text{size}(=\text{bandwidth}/\text{stepsize}+1)}, \\ f_2 = \dfrac{\sum_{i=1}^{\text{size}} (90 - |\varphi_{i1} - \varphi_{i2}|)^2}{\text{size}(=\text{bandwidth}/\text{stepsize}+1)}, \\ f_3 = \dfrac{\sum_{i=1}^{\text{size}} (90 - |\varphi_{i2} - \varphi_{i3}|)^2}{\text{size}(=\text{bandwidth}/\text{stepsize}+1)}, \\ f_4 = \dfrac{\sum_{i=1}^{\text{size}} (A_{i\max} - A_{i\min})}{\text{size}(=\text{bandwidth}/\text{stepsize}+1)}, \end{cases} \tag{4}$$

where the bandwidth is 0.68 THz–0.72 THz, stepsize is 0.005 THz, size is 8, φ_{ij} is the phase of the j_{th} state of the coded metasurface unit at the i_{th} frequency points, $A_{\max}$ and $A_{\min}$ are the maximum and minimum reflection amplitudes among the four states at the i_{th} frequency point respectively. Then, CST STUDIO SUITE (CST) is repeatedly called for simulating calculations. The *S*-parameters of each individual are exported to the main program for computing the fitness function values. It is then determined whether the termination condition of the algorithm (reaching the maximum number of iterations) is met. If not, optimization is conducted on each variable; otherwise, the optimal solution sequence of the current optimization parameters is output.

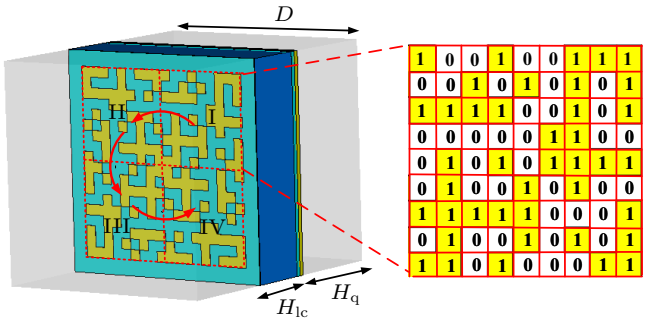


Fig. 4. The schematic coding metasurface unit with topological optimization design.

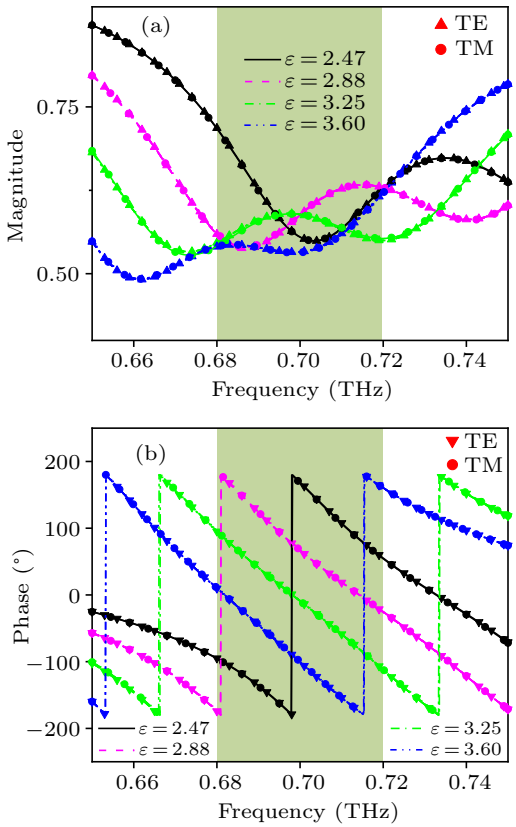


Fig. 5. Diagrams of (a) amplitude response and (b) phase response of the metasurface unit for TE and TM mode plane waves at LC effective dielectric constants ε of 2.47, 2.88, 3.25, and 3.60, respectively.

The optimized parameters of the metasurface unit obtained using the NSGA-II multi-objective optimization algorithm are as follows: $D = 210$ μm, $H_{\text{lc}} = 45$ μm, $H_{\text{q}} = 65$ μm.

The other two optimized dielectric constants of the LC are 2.88 and 3.25. The structure of the metasurface unit and its surface metal pattern are illustrated in Fig. 4.

In the case of a normally incident plane wave with linear polarization, the metasurface unit is simulated. Figure 5 illustrates the amplitude and phase responses of the metasurface unit in the frequency range of 0.65 THz–0.75 THz for TE and TM mode plane waves. It illustrates that within the frequency range of 0.68 THz–0.72 THz, the phase difference between adjacent curves is $90^\circ \pm 10^\circ$, and the reflection amplitude is greater than 0.55. Furthermore, the responses to TE and TM mode plane waves are nearly identical. Therefore, the designed coding metasurface unit can achieve polarization-independent 2-bit coding within the frequency range of 0.68 THz–0.72 THz.

3.2. Analysis of multifunctional coding metasurface simulation results

To improve the design efficiency and achieve flexible manipulation of THz waves, the array arrangement of the metasurface array is also inverse-designed using the NSGA-II multi-objective optimization algorithm. The metasurfaces array comprises 36×36 coding units, and the excitation electromagnetic wave is a linearly polarized plane wave. The CST is utilized to simulate the coding metasurface. Utilizing the Time-domain solver with local mesh refinement further enhances the accuracy of the simulation. In the experiment, the coded sequences generated by the optimization algorithm are first output to the FPGA board, with each channel of the FPGA independently connected to the units in the metasurface via ITO nanowires. Due to the low electrical resistance of the ITO nanowires, their presence has minimal impact on the scattering response of the metasurface.[23] The beam steering and vortex beam generation achieved by the coded metasurface are then measured using THz time-domain spectroscopy (THz-TDS).[10]

The optimization process for the array arrangements of the metasurface is illustrated in Fig. 2. The parameters including the period of the coding unit, the size of the metasurface, and the operating frequency are initialized. The fitness function is defined as

$$\min \begin{cases} f_1 = \left|\theta_{\text{real1}} - \theta_{\text{obj1}}\right| + \left|\varphi_{\text{real1}} - \varphi_{\text{obj1}}\right| + \dfrac{1}{M-1}\sum\limits_{i=0}^{M} P_{ri}, \\ f_2 = \left|\theta_{\text{real2}} - \theta_{\text{obj2}}\right| + \left|\varphi_{\text{real2}} - \varphi_{\text{obj2}}\right| + \dfrac{1}{M-1}\sum\limits_{i=0}^{M} P_{ri}, \\ \cdots, \\ f_N = \left|\theta_{\text{realN}} - \theta_{\text{obj}N}\right| + \left|\varphi_{\text{realN}} - \varphi_{\text{obj}N}\right| + \dfrac{1}{M-1}\sum\limits_{i=0}^{M} P_{ri}, \end{cases} \tag{5}$$

where $(\theta_{\text{obj}}, \varphi_{\text{obj}})$ is the preset target angle, $(\theta_{\text{real}}, \varphi_{\text{real}})$ is the real angle obtained by simulation, M is the number of beams in the far field, P_{ri} $(i = 0, 1, \ldots, M)$ is the power of the i_{th} secondary beam, and N is the number of target beams. The number of optimization parameters is set to 36×36, the population size is set to 100, and the maximum number of iterations is set to 300. Each individual is then substituted into Eq. (2), and the fitness function value is calculated.

3.2.1. Beam steering

For the beam steering, to evaluate the error between the simulation results obtained from the reverse design and the preset target, the angle error $E(\theta, \varphi)$ between the actual simulation results and the main lobe of the preset target is defined as follows:

$$E(\theta, \varphi) = \frac{1}{N}\sum\nolimits_{\text{i}=1}^{N} \frac{1}{2} \cdot \left[\left|\theta_{\text{real}} - \theta_{\text{obj}}\right| + \left|\varphi_{\text{real}} - \varphi_{\text{obj}}\right|\right]. \tag{6}$$

(i) Single-beam steering

The beam steering of a single beam at 0.70 THz under different $(\theta_{\text{obj}}, \varphi_{\text{obj}})$ are studied. The simulation results for target angles of (7°, 30°), (15°, 130°), (25°, 230°), and (35°, 330°) are illustrated in Fig. 6. Figures 6(a)–6(d) illustrate the metasurface array arrangements obtained using the NSGA-II multi-objective optimization algorithm at the target angles, figures 6(e)–6(h) illustrate the corresponding three-dimensional far-field scattering results for each array for TE mode, and figures 6(i)–6(l) illustrate the corresponding results for TM mode.

The calculated values of $E(\theta, \varphi)$ for the four cases are all 0° for the TE mode, while they are 0.05°, 0.15°, 0°, and 0° for the TM mode, all of which are less than 0.2°. The small angle error indicates that the simulation results are consistent with the preset target. The 3-dB beamwidth of the target beam is approximately 2.9°, indicating a high level of directivity.

It can be observed that some sidelobes are present in addition to the main target beam in Fig. 6. This is due to the incomplete uniformity of the reflection amplitudes among the four coding states, the phase differences between adjacent states not being strictly 90°, and the phase discontinuities of the metasurface units. The energy differences between the main target beam and the maximum energy of the sidelobes are 10.1 dB, 9.2 dB, 6 dB, and 3.2 dB for the TE mode, the corresponding values are 9.8 dB, 9.2 dB, 6.1 dB, and 3.1 dB for the TM mode, indicating effective control for TE/TM mode. The research indicates that when the elevation angle of the target beam exceeds 35°, the sidelobe energy approaches or even surpasses that of the target beam. The range of elevation angle control is constrained by the ratio between the period of the coding metasurface unit and its operational wavelength.

Therefore, the proposed reconfigurable coding metasurface, which is reverse-designed by the NSGA-II multi-objective optimization algorithm, enables arbitrary angle control of a single beam within the range of elevation angles up to 35° and azimuthal angles within 360° for the TE and TM modes.

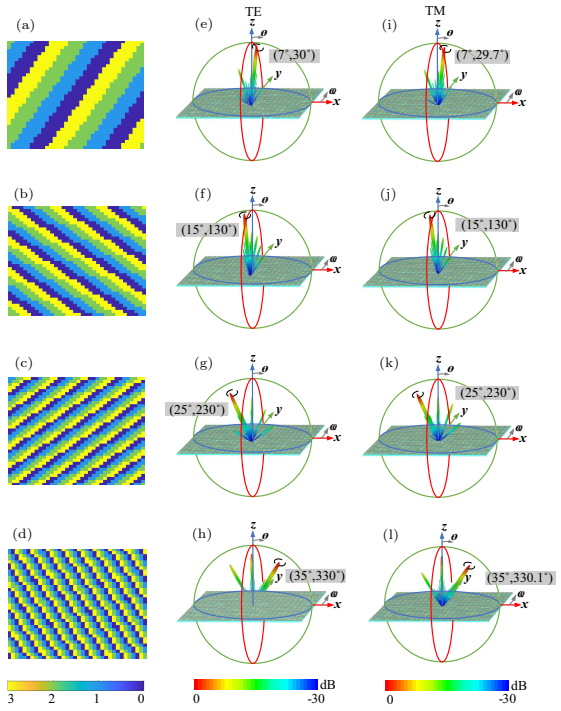


Fig. 6. (a)–(d) Array coding sequence (θ_{obj}, φ_{obj}) for (7°, 30°), (15°, 130°), (25°, 230°), and (35°, 330°) respectively; (e)–(h) the corresponding far-field scattering results for TE mode; (i)–(l) the corresponding far-field scattering results for TM mode.

(ii) Multi-beam steering

The multi-beam steering of coding metasurfaces at different elevations and azimuth angles has been studied. Simulations for the independent steering of multi-beam ($N = 2$, 3, 4, 5) at different target angles have been conducted, and the results are illustrated in Fig. 7.

The calculated values of $E(\theta, \varphi)$ for the four cases are 0.05°, 0.06°, 0.24°, and 0.17° for the TE mode, while they are 0.07°, 0.12°, 0.15°, and 0.18° for the TM mode, all of which are less than 0.25°. The differences between the minimum energy of the target beam and the maximum energy of the sidelobes are 5.1 dB, 4.2 dB, 4 dB, and 5.1 dB for the TE mode, the corresponding values are 5 dB, 4.3 dB, 4.1 dB, and 5.2 dB for the TM mode, indicating a high efficiency in multi-beam steering. Additionally, the differences between the highest and lowest scattering amplitudes of the main lobes in the target beam are 0.98 dB, 0.43 dB, 1.05 dB, and 0.4 dB for the TE mode, while they are 0.91 dB, 0.45 dB, 1 dB, and 0.42 dB for the TM mode. This indicates that the intensity distribution of the target beam is relatively uniform.

Therefore, the proposed reconfigurable coding metasurface can achieve independent control over different numbers of target beams within the elevation angle range of 35° and azimuth range of 360° for the TE and TM modes. Since multi-beam steering can cover multiple target areas simultaneously and scan objects at various angles, it holds significant potential for applications in phased array radar.

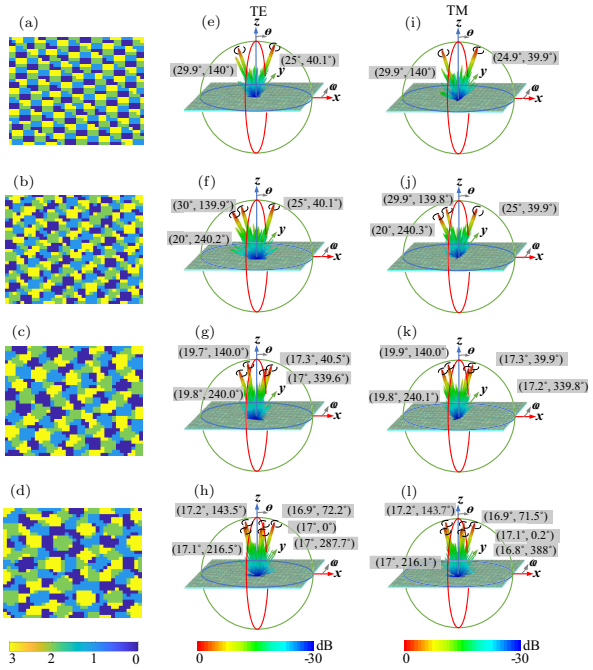


Fig. 7. (a), (e), (i) Array coding sequence and far-field scattering results of (θ_{obj}, φ_{obj}) for two beams (25°, 40°), (30°, 140°), respectively; (b), (f), (j) array coding sequence and far-field scattering results of (θ_{obj}, φ_{obj}) for three beams (25°, 40°), (30°, 140°), and (20°, 240°), respectively; (c), (g), (k) array coding sequence and far-field scattering results of (θ_{obj}, φ_{obj}) for four beams (17°, 40°), (20°, 140°), (20°, 240°), and (17°, 340°), respectively; (d), (h), (l) array coding sequence and far-field scattering results of (θ_{obj}, φ_{obj}) for five beams (17°, 0°), (17°, 72°), (17°, 144°), (17°, 216°), and (17°, 288°), respectively.

(iii) Broadband capability of beam steering

Taking three beams as an example, the broadband characteristics of beam steering for the coding metasurface within the frequency range of 0.68 THz–0.72 THz are studied. Figure 8 illustrates the array arrangement of the coding metasurface and the simulation results at frequencies of 0.68 THz, 0.70 THz, and 0.72 THz.

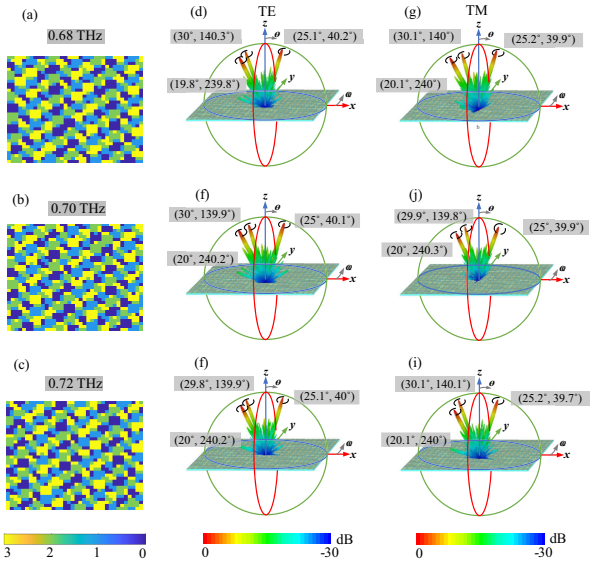


Fig. 8. Array coding sequence of (θ_{obj}, φ_{obj}) for three beams (25°, 40°), (30°, 140°), and (20°, 240°) at (a) 0.68 THz, (b) 0.70 THz, and (c) 0.72 THz, respectively; (d)–(f) the corresponding far-field scattering results for TE mode; (g)–(i) the corresponding far-field scattering results for TM mode.

The calculated values of $E(\theta,\varphi)$ for the three cases are 0.16°, 0.06°, and 0.1° for the TE mode, while they are 0.08°, 0.12°, and 0.18° for the TM mode, all of which are less than 0.2°. The differences between the minimum energy of the target beam and the maximum energy of the sidelobes are 4.3 dB, 4.2 dB, and 4.4 dB for the TE mode, the corresponding values are 4.2 dB, 4.3 dB, and 4.5 dB for the TM mode. The differences between the highest and lowest scattering amplitudes of the main lobes in the target beam are 0.44 dB, 0.43 dB, and 0.42 dB for the TE mode, while they are 0.42 dB, 0.45 dB, and 0.44 dB for the TM mode. Therefore, the proposed reconfigurable coding metasurface can achieve flexible beam steering within the frequency range of 0.68 THz–0.72 THz for the TE and TM modes.

3.2.2. OAM vortex beam

Mode purity is commonly used to quantitatively analyze the generated vortex beams, and it refers to the ratio of the energy of each mode to the total energy. To achieve mode purity, a Fourier transform of the circular electric field in the main lobe of the generated vortex beam is performed to obtain the OAM spectrum. Subsequently, normalization of each mode is conducted to determine the mode purity for the corresponding mode. The OAM spectrum calculation formula is as follows:[24]

$$A_l = \frac{1}{2\pi}\int_0^{2\pi} \psi(\varphi)\cdot \mathrm{e}^{-\mathrm{i}l\varphi}\,\mathrm{d}\varphi, \tag{7}$$

where A_l is the amplitude of the corresponding mode, and $\psi(\varphi)$ is the circular electric field.

(i) Generation of the single-OAM vortex beam

The generation of single vortex beams with different topological charges using coding metasurfaces is studied at 0.70 THz. The simulation results are illustrated in Fig. 9.

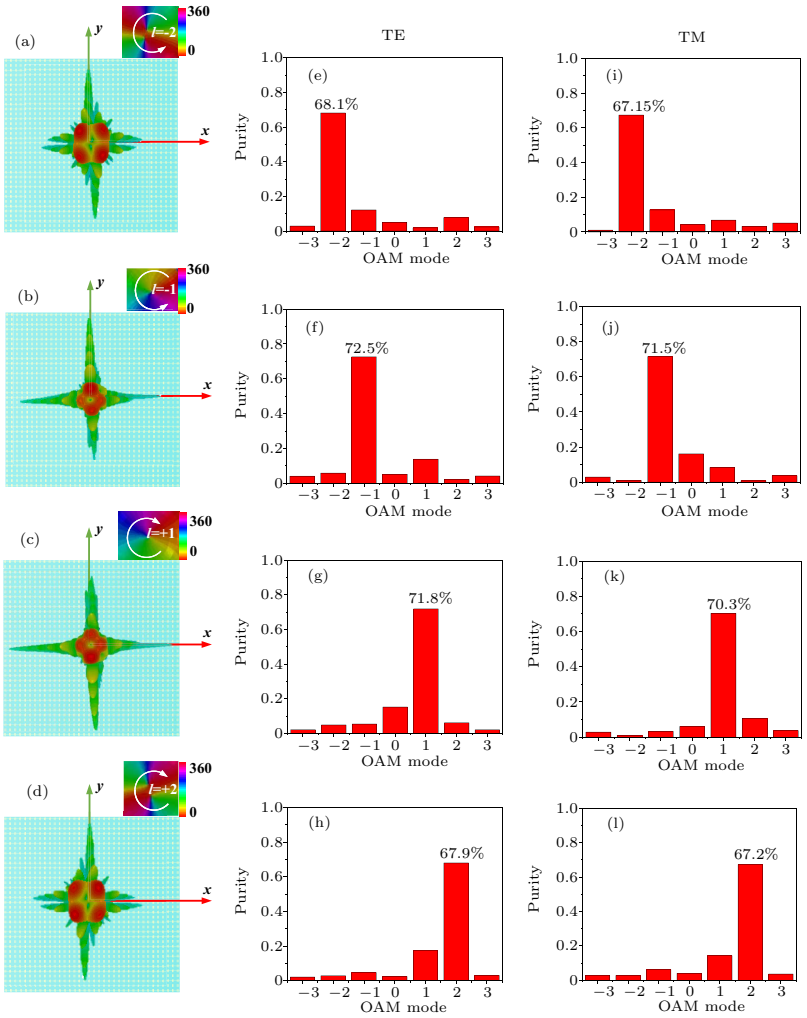


Fig. 9. Far-field scattering intensity and phase distribution results at 0.70 THz for (a)–(d) $l = \pm1, \pm2$; (e)–(h) the corresponding pattern purity distribution diagrams for TE mode, (i)–(l) the corresponding pattern purity distribution diagrams for TM mode.

Figures 9(a)–9(d) illustrate the far-field scattering results and phase distributions for the generation of topological charge $l = \pm1, \pm2$ respectively. It can be observed that the electric field intensity of the vortex beam exhibits a circular distribution, with a depression at the center where the electric field intensity is zero. When the topological charge is $l = \pm1$,

± 2 the phases undergo 1–2 clockwise or counterclockwise cycles from 0° to 360° respectively, which are consistent with the characteristics of the vortex beam. Figures 9(e)–9(l) illustrate the corresponding mode purities respectively. The mode purities for the topological charge $l = \pm 1, \pm 2$ are 71.8%, 72.5%, 67.9%, and 68.1% for the TE mode, while they are 70.3%, 71.5%, 67.2%, and 67.1% for the TM mode. This indicates that the coding metasurface is capable of generating a vortex beam with good performance.

(ii) Generation of the multi-OAM vortex beam

Since vortex beams are obtained by convolving the vortex phase with ordinary beams, theoretically, by convolving the vortex phase corresponding to different topological charge ($l = -2, -1, +1$, and $+2$) with the array arrangement of a certain target angle (θ_{obj}, φ_{obj}) reverse designed by the NSGA-II multi-objective optimization algorithm, flexible and diverse generation of single- and multi-vortex beams with elevation angles within a 35° range and azimuth angles within a 360° range achieved with polarization independence over the frequency range of 0.68 THz–0.72 THz.

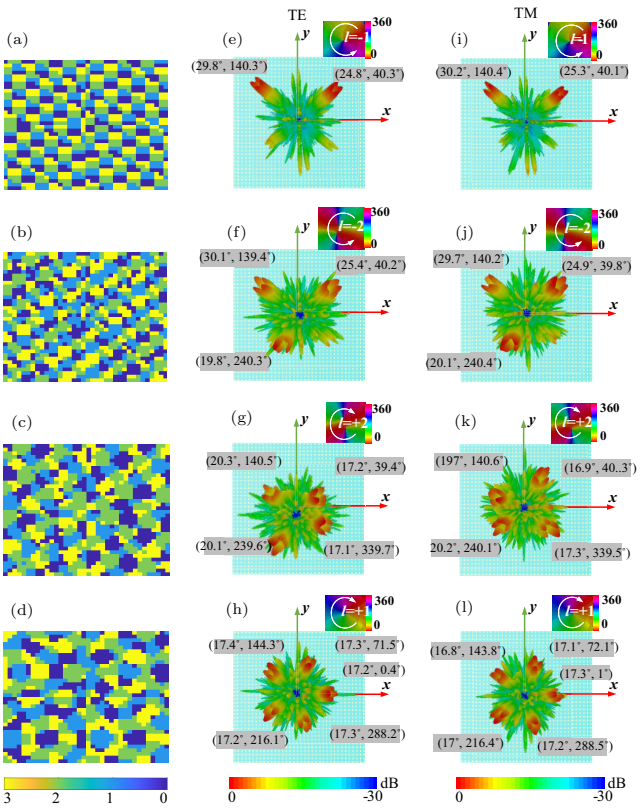


Fig. 10. (a), (e), (i) Array coding sequence and far-field scattering results of (θ_{obj}, φ_{obj}) for two vortex beams (25°, 40°), (30°, 140°), respectively; (b), (f), (j) array coding sequence and far-field scattering results of (θ_{obj}, φ_{obj}) for three vortex beams (25°, 40°), (30°, 140°), and (20°, 240°), respectively; (c), (g), (k) array coding sequence and far-field scattering results of (θ_{obj}, φ_{obj}) for four vortex beams (17°, 40°), (20°, 140°), (20°, 240°), and (17°, 340°), respectively; (d), (h), (l) array coding sequence and far-field scattering results of (θ_{obj}, φ_{obj}) for five vortex beams (17°, 0°), (17°, 72°), (17°, 144°), (17°, 216°), and (17°, 288°), respectively.

Taking the array in multi-beam steering as example, the simulation results of multi-vortex beams with different topological charges are illustrated in Fig. 10. From the three-dimensional far-field scattering results, it can be observed that each multi-vortex beam generated by the metasurface satisfies the characteristics of a vortex beam with different topological charges. The angular errors $E(\theta, \varphi)$ are 0.25°, 0.3°, 0.29°, and 0.29° for the TE mode, the corresponding values are 0.25°, 0.21°, 0.3° , and 0.3° for the TM mode. The angular errors are all around 0.3°, which demonstrates effective control over the vortex beam with good accuracy.

(iii) Broadband capability of vortex beam generation

Taking three vortex beams as an example, the broadband characteristics of vortex beam generation for the coding metasurface within the frequency range of 0.68 THz–0.72 THz are studied.

Figure 11 illustrates the array arrangement of the coding metasurface and the simulation results at frequencies of 0.68 THz, 0.70 THz, and 0.72 THz. The calculated values of $E(\theta, \varphi)$ for the three cases are 0.23°, 0.3°, and 0.25° for the TE mode, while they are 0.33°, 0.22°, and 0.3° for the TM mode, all of which are less than 0.4°.

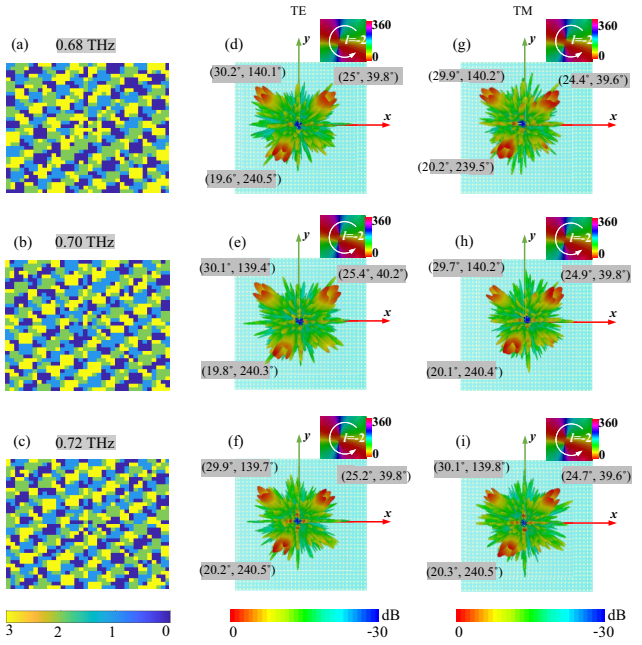


Fig. 11. Array coding sequence of (θ_{obj}, φ_{obj}) for three vortex beams (25°, 40°), (30°, 140°), and (20°, 240°) at (a) 0.68 THz, (b) 0.70 THz, and (c) 0.72 THz, respectively; (d)–(f) the corresponding far-field scattering results for TE mode; (g)–(i) the corresponding far-field scattering results for TM mode.

Therefore, the proposed reconfigurable coding metasurface can generate single and multi-vortex beams with different topological charges and beam numbers within the frequency range of 0.68 THz–0.72 THz. For the generation of multi-vortex beams, the generation angles of each vortex beam can still be independently controlled, offering high flexibility and diversity. This makes it promising for applications in vortex radar and three-dimensional synthetic aperture radar (SAR) imaging.

4. Conclusion

A broadband polarization-independent THz multifunctional coding metasurface based on topological optimization is proposed in this paper, which achieves polarization-independent 2-bit coding within the range of 0.68 THz–0.72 THz. The array arrangements of the metasurface have been reverse-designed using the NSGA-II multi-objective optimization algorithm, which improves the design efficiency and achieves beam assignment and vortex beam generation. The results indicate that, for beam steering, flexible steering of both single- and multi-beam can be achieved within the 35° elevation angle range and 360° azimuth range in this frequency band. Moreover, the elevation and azimuth angles of each beam in the multi-beam steering can be independently controlled. For vortex beam generation, vortex beam with topological charges $l = \pm 1, \pm 2$ and mode purities greater than 67% can be generated. Multi-vortex beams can be generated within an elevation angle range of 35° and an azimuth range of 360° can be generated. This provides flexibility and diversity in vortex beam generation. Therefore, this reverse-designed multifunctional reconfigurable metasurface holds promising application potential in fields such as THz communication, phased array radar, and vortex radar.

Acknowledgements

Project supported by the Open Fund of Wuhan National Research Center for Optoelectronics (Grant No. 2022WNLOKF012) and the National College Students Innovation and Entrepreneurship Training Program (Grant No. 2023102930147).

References

[1] Cui T J, Qi M Q, Wan X, *et al*. 2014 *Light: Science & Applications* **3** 218
[2] Lai P T, Li Z L, Wang W, *et al*. 2022 *Chin. Phys. B* **31** 098102
[3] Yu J Y, Zheng Q R, Zhang B, *et al*. 2022 *Chin. Phys. B* **31** 090704
[4] Hong J, Ni M Y, Zhang Z P, Hu Z D, Wang J C, Shen X P, Wang X, Li M M and Khakhomov Sergei 2024 *Nanophotonics* **14** 13
[5] Zhang B L, Hu Z D, Wu J J, *et al*. 2023 *Opt. Lett.* **48** 2409
[6] Bai T R, Li Q, Wang Y Q, *et al*. 2021 *Opt. Express* **29** 25270
[7] Jing X F, Ke Y H, Tian Y, *et al*. 2020 *IEEE Access* **8** 164795
[8] Hu X L, Yang Q L, Ba L L, *et al*. 2023 *Opt. Lett.* **48** 908
[9] Ba L L, Yang Q L, Yang J C, *et al*. 2024 *Opt. Lett.* **49** 5075
[10] Liu C X, Yang F, Fu X J, *et al*. 2021 *Adv. Opt. Mater.* **9** 2100932
[11] Si L M, Tang P C and Lv X 2022 *ZTE Technology* **28** 13
[12] Zhang H, Huang J, Tian M, *et al*. 2023 *Opt. Commun.* **527** 128958
[13] Zhang Y J, Luan J Q, Li C L, *et al*. 2024 *Acta Opt. Sin.* **44** 1124002
[14] Luan J Q, Zhang Y J, Chen Y, *et al*. 2024 *Acta Phys. Sin.* **73** 144204 (in Chinese)
[15] Lv E P, Wang W G, Liu S Y, Pan T Y, Zhu C X and Wang H M 2023 *Conference on Lasers and Electro-Optics (CLEO)* pp. 1–2
[16] Wang W G, Lv E P, Hou Y Z, *et al*. 2022 *Asia Communications and Photonics Conference (ACP)* 50
[17] Cheng G, Si L M, Tang P C, *et al*. 2022 *Opt. Express* **30** 41340
[18] Zhao S D, Zhang L N, Han P, *et al*. 2024 *Small (Weinheim an der Bergstrasse, Germany)* **20** 2308349
[19] Han D, Ma Z Y, Wang J L, *et al*. 2022 *Chin. J. Lasers* **49** 1714001
[20] Sui S, Ma H, Wang J F, *et al*. 2019 *J. Phys. D: Appl. Phys.* **52** 035103
[21] Deng G, Hu H, Mo H, *et al*. 2022 *Opt. Express* **30** 22550
[22] Gao S, Yang J, Wang P, *et al*. 2018 *Appl. Sci.* **8** 2528
[23] Zhang G Z, Li K W, Xu L, *et al*. 2024 *IEEE Antennas and Wireless Propagation Letters* **23** 2066
[24] Li G Q, Shi H Y, Liu K, *et al*. 2021 *Acta Phys. Sin.* **70** 188701 (in Chinese)